

Optically computed phase microscopy for quantitative dynamic imaging of label-free cells and nanoparticles

XUAN LIU,^{1,*} ZHAOXIONG WAN,²  YUANWEI ZHANG,² AND YUWEI LIU¹

¹Department of Electrical and Computer Engineering, New Jersey Institute of Technology, University Heights, Newark, New Jersey 07102, USA

²Department of Chemistry and Environmental Science, New Jersey Institute of Technology, University Heights, Newark, New Jersey 07102, USA

*xliu@njit.edu

Abstract: Numerous drug delivery systems based on nanoparticles have been developed, such as those used in BioNTech/Pfizer's and Moderna's Covid vaccines. Knowledge on mechanical interactions between cells and nanoparticles is critical to advance the efficiency and safety of these drug delivery systems. To quantitatively track the motion of cell (transparent) and nanoparticles (nontransparent) with nanometer displacement sensitivity, we investigate a novel imaging technology, optically computed phase microscopy (OCPM) that processes 3D spatial-spectral data through optical computation. We demonstrate that OCPM has the capability to image the motion of cells and magnetic nanoparticles that are mechanically excited by an external magnetic field, quantitatively and in the en face plane.

© 2021 Optica Publishing Group under the terms of the [Optica Open Access Publishing Agreement](#)

1. Introduction

Numerous nanoparticle drug delivery systems have been investigated in preclinical studies and clinical trials [1,2]. BioNTech/Pfizer's and Moderna's Covid vaccines both use lipid nanoparticles as mRNA carriers [3]. Quantitatively imaging the mechanical interactions between cells and nanoparticles are critical to advance the efficiency and safety of drug delivery using nanoparticles [4]. Phase-resolved optical imaging technologies provide a label-free approach to image the structure and dynamics of cells, by deriving the contrast from the phase of optical wave. However, classical phase imaging methods, including phase contrast (PC) microscopy and differential interference contrast (DIC) microscopy [5,6], are qualitative and do not provide quantitative phase measurement. Quantitative phase measurement has been achieved in phase-resolved optical coherence tomography (OCT) and quantitative phase imaging (QPI) [7–17]. These techniques either have a limited spatiotemporal resolution or require the sample to be a thin and transparent phase object. Another technology worth mentioning is Optical diffraction tomography (ODT) that utilizes computer algorithms to reconstruct the spatial distribution refractive index. In ODT, multiple interferometric measurements under different illumination conditions are needed [18–20]. To address the unmet need for dynamic imaging of cell-nanoparticle interaction with high spatiotemporal resolution, we investigate a novel technique, optically computed phase microscopy (OCPM). OCPM takes an innovative optical computation strategy to process 3D spatial-spectral data before 2D photon detection and allows depth resolved phase measurement through snapshot detection. Optical computation has been used to manage massive data, for applications such as OCT imaging and single pixel imaging [21–24]. OCPM uses a spatial light modulator (SLM) to alter light intensity with high spatial and value precision and addresses two significant challenges in phase imaging. First, optical computation achieves depth resolution, by computing the inner product between the interferometric spectrum and a Fourier basis projected

by the SLM. Second, optical computation imposes a sinusoidal modulation on the interferometric term of optical signal, resulting in a waveform that facilitates phase quantification from a real measurement. OCPM is similar to OCT in its use of interferometry for the measurement of optical field. However, unlike conventional OCT system that prioritizes B-scan, OCPM performs phase resolved snapshot imaging in the *en face* plane. This is a desirable feature for imaging cultured cells and their interaction with nanoparticles. Moreover, current optical imaging systems including OCT perform signal processing after data acquisition while OCPM data is processed optically before detection. In OCPM, the signal processing function of the computer is partially replaced by the optical computation module. More importantly, the optical computation module processes the 3D spatial-spectral (x - y - k) data optically. Afterwards, the 3D data collapses for 2D detection. Optical computation plays a significant role in reducing the dimension of data, enabling depth resolved imaging and quantitative phase measurement.

With its unique imaging capabilities, OCPM has the potential to advance the knowledge on the mechanical interaction between cells and nanoparticles, and lead to nanoparticle drug delivery systems with improved efficacy and safety. The spatial resolution and displacement sensitivity of OCPM makes it an ideal candidate to image the dynamic interaction between cells and nanoparticles. First, OCPM does not rely on labeling reagents, and allows cell movements and behaviors to remain unaffected during the imaging process. Second, OCPM allows quantitative phase measurement and has the capability to track subtle motion with nanoscale displacement sensitivity. Third, with depth resolution derived from low coherence interferometry and optical computation, OCPM operated in a reflective mode can image transparent and non-transparent objects. This is critical for imaging cells in a complicated environment where non-transparent objects such as nanoparticles exist. Moreover, OCPM also has the capability to resolve a thin layer from a bulk object. Therefore, OCPM is translatable to *in vivo* studies on animals or human subjects.

In this study, we build the OCPM system and validate its performance. The OCPM system allows depth resolved quantitative phase imaging in the *en face* plane, and achieves a $1\ \mu\text{m}$ lateral resolution, $8.4\ \mu\text{m}$ axial resolution, $2.8\ \text{nm}$ displacement sensitivity. We use the OCPM system to quantitatively study the dynamics of cells and magnetic nanoparticles, with motion introduced by an external magnetic field. We focus on quantifying motion in axial direction through Doppler analysis, while transverse motion can be quantified through speckle tracking in the future. Notably, the magnetic nanoparticles are not transparent and their axial motion cannot be quantified using a common phase imaging platform operated on transmission mode.

2. Principle

Figure 1(a) shows the configuration of the OCPM system. The sample is represented by the complex field reflectivity: $i_{\text{sample}}(x,y,z)=A(x,y,z)e^{i\phi(x,y,z)}$, where z indicates the direction of light propagation, (x,y) is the transverse coordinate, $A(x,y,z)$ is the amplitude and $\phi(x,y,z)$ is the phase. To measure the field reflectivity, the OCPM system uses a low coherent light source to illuminate a Michelson interferometer that has a reference and a sample arm. The output from the Michelson interferometer is interfaced with an optical computation module detailed in Fig. 1(b). The optical computation module consists of a diffraction grating, a lens, and a reflective spatial light modulator (SLM) that has a wide range of applications in optical imaging [25]. As illustrated in Fig. 1(c), through the grating and the lens, $i(x,y,k)$ (wavenumber $k=2\pi/\lambda$) from different y coordinate is mapped to different rows of the SLM. The spectrum hitting the SLM has a linear shift within the row depending on the x coordinate. On the other hand, each pixel of the 2D SLM sees superposition of signal from different (x,k) combinations (Fig. 1(d)). To achieve depth resolution, the SLM modulates interferometric spectra along k dimension sinusoidally and the camera detects light without spectral discrimination. This effectively selects signal from the depth determined by the Fourier basis projected to the SLM, similar to the strategy

utilized in our previous study for scanning free volumetric imaging [21]. Notably, the SLM also imposes modulation along y dimension. This allows us to extract the complex field reflectivity from a real measurement and facilitates phase extraction. The key to achieve depth resolved quantitative phase imaging is to utilize a strategically designed pattern $f(k,y)$ at the SLM for optical computation.

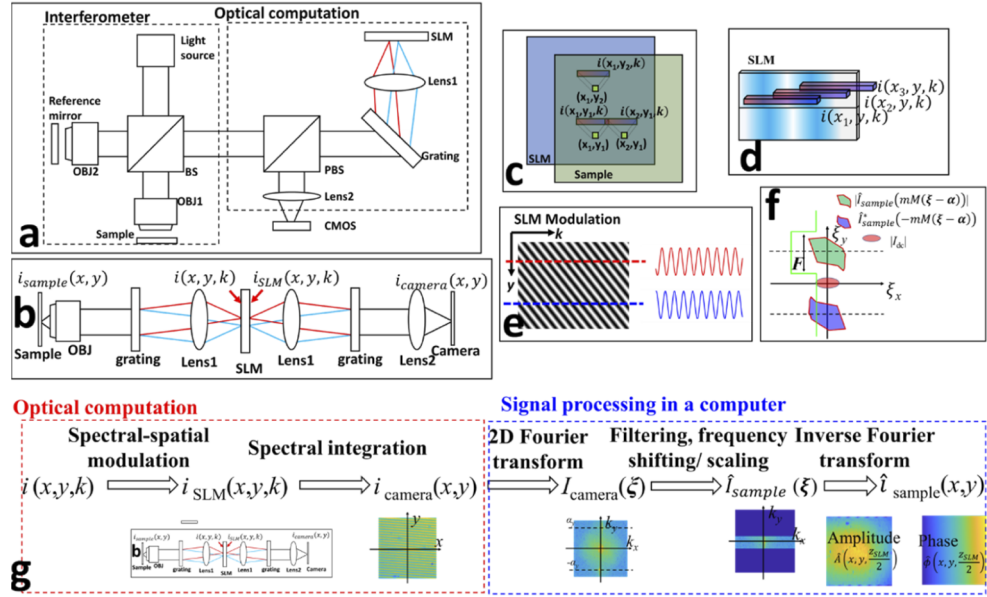


Fig. 1. (a) OCPM system; (b) the optical computation module; (c) the mapping between pixels in the sample plane and spectra seen by the SLM; (d) each pixel of the SLM sees signal from different combinations of (x,k) ; (e) light modulation along k and y dimension; (f) $I_{camera}(\xi)$ in spatial frequency domain; (g) signal processing procedure for OCPM.

To further illustrate the principle of OCPM, we consider the 3D spatial-spectral data cube $i(x,y,k)$ output from the interferometer. Assuming the axial location of the reference reflector to be 0 and the field reflectivity of the reference mirror be 1, $i(x,y,k)$ is found to be Eq. (1) where $S_0(k)$ is the source spectrum, and $\text{Re}()$ indicates to take the real part of a complex function. $i(x,y,k)$ is modulated by the SLM with a pattern $f(k,y)$ (Eq. (2) and Fig. 1(e)), resulting in $i_{SLM}(x,y,k) \propto f(k,y)i(x/M,y/M,k)$ where M is the magnification from the sample plane to the SLM. Reflected by the SLM, $i_{SLM}(x,y,k)$ goes through the grating for the second time and is detected by the camera without spectral discrimination. The signal detected by the camera, $i_{camera}(x,y)$, is the integral of i_{SLM} over k , and is found to be Eq. (3) where ε is a constant accounting for system efficiency, η is a constant representing detector sensitivity, m is the magnification from the SLM to the camera, $r_0(x,y)$ is a low frequency term, $r_s(z) = \gamma_0(z) \otimes A^*(\frac{x}{mM}, \frac{y}{mM}, z)$, \otimes represents convolution along z dimension, and $\gamma_0(z)$ represents the axial point spread function (PSF) that is related to source spectrum $S_0(k)$ through Fourier transform. According to second row of Eq. ((3)), the sinusoidal component along k dimension in $f(k,y)$ ensures the signal comes from $z_{SLM}/2$, and the sinusoidal component along y dimension ensures creates a waveform ($\exp(j\alpha_y y/m - \phi)$) to facilitate phase extraction.

$$i(x,y,k) = S_0(k)(|A(x,y,z)|^2 + 1) + 2S_0(k)\text{Re}\left[\int A(x,y,z)e^{2jkz}dz\right] \quad (1)$$

$$f(k,y) = 1 + \cos(kz_{SLM} + \alpha_y y) \quad (2)$$

$$\begin{aligned}
 i_{camera}(x, y) &= \eta \int i_{SLM} \left(\frac{x}{m}, \frac{y}{m}, k \right) dk = \varepsilon \eta \int i \left(\frac{x}{mM}, \frac{y}{mM}, k \right) f \left(k, \frac{y}{m} \right) dk \\
 &= r_0(x, y) + \frac{1}{2} e^{j(\alpha_y \frac{y}{m} - \phi)} r_s(2z - z_{SLM}) + \frac{1}{2} e^{-j(\alpha_y \frac{y}{m} - \phi)} r_s^*(2z - z_{SLM})
 \end{aligned} \quad (3)$$

To extract the phase, we consider $I_{camera}(\xi)$, the 2D Fourier transform of $i_{camera}(x, y)$. Utilizing the Fourier transform property of a modulated signal, we find $I_{camera}(\xi)$ to be Eq. (4), where ξ is the spatial frequency vector $\xi = [\xi_x, \xi_y]'$, $\alpha = [0, \alpha_y/m]'$, $R_0(\xi)$ is the 2D Fourier transform of $r_0(x, y)$, and \hat{I}_{sample} is defined in Eq. (5). In Eq. (4), the first term is located at the origin of the spatial frequency plane, while the second and third terms are displaced from each other, as illustrated in Fig. 1(f). Therefore, $\hat{I}_{sample}(\xi)$ can be obtained from $I_{camera}(\xi)$, following spatial frequency domain filtering, frequency shifting and scaling. Spatial domain signal, $\hat{i}_{sample}(x, y)$ (Eq. (6)), is thus obtained by applying inverse Fourier transform on $\hat{I}_{sample}(\xi)$.

$$I_{camera}(\xi) = R_0(\xi) + \hat{I}_{sample}(mM(\xi - \alpha)) + \hat{I}_{sample}^*(-mM(\xi - \alpha)) \quad (4)$$

$$\hat{I}_{sample}(\xi) = \gamma_0(2z - z_{SLM}) \otimes (I_{sample}(\xi, 2z - z_{SLM})) \quad (5)$$

$$\hat{i}_{sample}(x, y) = \gamma_0(2z - z_{SLM}) \otimes (i_{sample}(x, y, 2z - z_{SLM})) \quad (6)$$

Although $\hat{i}_{sample}(x, y)$ does not explicitly depend on depth, the coherence gating of OCPM (convolution with the axial PSF in Eq. (6)) effectively selects signal at depth $z_{SLM}/2$. Therefore, the amplitude and phase of the sample at depth $z_{SLM}/2$ can be estimated from \hat{i}_{sample} : $\hat{A}(x, y, z_{SLM}/2) = |\hat{i}_{sample}(x, y)|$ and $\hat{\phi}(x, y, z_{SLM}/2) = \arg(\hat{i}_{sample}(x, y))$.

In summary, OCPM processes the 3D spatial-spectral data $i(x, y, k)$ in two steps, as summarized by Fig. 1(g). Before detection, the optical computation module calculates the inner product between $i(x, y, k)$ and a Fourier basis (sinusoidal modulation along k followed by integration with regard to k) to achieve depth resolution, and creates modulation in y direction to facilitate phase extraction. After detection by a 2D camera, the signal processing is accomplished in a computer which performs 2D Fourier transform, bandpass filtering, frequency shifting/scaling, inverse Fourier transform, and amplitude and phase extraction.

Theoretically, the axial resolution of OCPM is determined by coherence gating (Eq. ((6))) and is limited by the bandwidth of the light source in a same manner as conventional OCT imaging. The lateral resolution in x dimension is limited by the mechanisms as conventional microscopy, such as lens aberration or diffraction. In y dimension, the lateral resolution is also determined by spatial frequency domain filtering (Fig. 1(f)). The full bandwidth of spatial frequency domain signal after filtering is $\alpha_y/(m)$ and the smallest structure resolvable in y direction has a dimension of $\delta y_{\text{filt}} = 1/(\alpha_y/m)$. A denser modulation imposed to the SLM will lead to a stronger resolving power in y dimension.

3. Experiments

We built the OCPM system as illustrated in Fig. 1(a). We used a mounted LED (Thorlabs) with central wavelength $\lambda_0 = 730$ nm and bandwidth $\delta\lambda = 40$ nm as the broadband source. In the Michelson interferometer, the input of the light source is directed to the reference arm and sample arm by a beam splitter. We used a pair of water dipping objectives (40X Nikon CFI APO NIR Objective, NA = 0.8) in front of the sample and reference reflector. In the optical computation module, the interferometric spectrum was dispersed by a 1200/mm grating, modulated by a 2D SLM (Holoeye LC-R 720). The light goes through the grating for a second time after it is reflected by the SLM. The signal is detected by a CMOS camera (Basler acA2000). The achromatic doublet lenses in front of the SLM and in front of the CMOS had a focal length of 400 mm and 200 mm, respectively. Notably, a polarized beam splitter (PBS) was inserted before the optical computation module to ensure amplitude modulation by the SLM. The exposure

time of the camera was adjusted to fully utilize the dynamic range of the detector. To impose sinusoidal modulation to the light spectrum, we experimentally characterized the mapping (p) between the pixel value of the synthesized mask (v_{syn}) and the actual amplitude modulation value (v_{actual}): $v_{\text{actual}} = p(v_{\text{syn}})$, and used this mapping to create a pattern to eliminate the nonlinearity of SLM [21]. We used Matlab 2021 to perform signal processing. We followed procedures in Fig. 1(g) to obtain the amplitude and phase images and did not perform image enhancement or noise suppression for 2D images presented. We used HeLa cells for cellular imaging. HeLa cells were cultured in Dulbecco's Modified Eagle Medium supplemented with 10% fetal bovine serum, 1% penicillin/streptomycin at 37 °C in a humidified 5% CO₂ incubator. For imaging, cells were seeded on confocal dish (MatTek) at the density of 4×10^4 cells per dish. Magnetic nanoparticles were prepared by hydrolyzing iron salts in alkaline solutions at room temperature using a reported method [26]. Ferrous chloride and ferric chloride were used as iron salts (0.05 mol/L), and mixed with 1,6-hexanedimaine solution (0.25 mol/L). After vigorous stirring for 24 hours, the precipitation was collected by filtration and washing with ultrapure water. The black solids were then coated with Pluronic F-127 to improve water solubility and reduce cell toxicity.

4. Results

We characterized the axial resolution, lateral resolution, and phase sensitivity of the OCPM system. To validate optical computation strategy that facilitates phase extraction, we placed a mirror at the sample arm, projected different patterns at the SLM (Eq (2) with $z_{\text{SLM}} = 90 \mu\text{m}$ and $\alpha_y = 0, 0.63 \mu\text{m}^{-1}, 1.26 \mu\text{m}^{-1}$, and adjusted the optical path length of the sample arm to maximize the contrast of the interference fringe such that $z = z_{\text{SLM}}/2 = 45 \mu\text{m}$. Figure 2(a) – (c) show measurements taken by the camera. When $\alpha_y = 0$, a waveform does not exist in the measurement (Fig. 2(a)), suggesting it is impossible to extract the phase quantitatively from the real measurement. As α_y increases, the measurements show increasingly denser fringe along y dimension, suggesting larger frequency shift in spatial frequency domain. We performed 2D Fourier transform on OCPM measurements and extracted the amount of frequency shift. In Fig. 2(d), we correlate the value of α_y used to generate the modulation pattern, and the frequency shift measured (α_{measured}) after 2D Fourier transform. Consistency between α_y and α_{measured} can be clearly observed. Notably, for all the measurements described subsequently in this manuscript, we used $\alpha_y = 2.51 \mu\text{m}^{-1}$. To evaluate the depth resolution of OCPM, we followed the standard practice and used a mirror as the sample that had an impulse reflectivity profile (delta function along z dimension). We maintained the mirror at the same depth $z = 45 \mu\text{m}$, and created modulation patterns at the SLM according to Eq. (3) with different values of z_{SLM} . We obtained amplitude images and obtained the axial point spread function (PSF), using the amplitude signal at the center of the field of view (Fig. 2(e)). We assumed a Gaussian PSF, because the spectrum captured was approximately Gaussian, and the PSF is related to the source spectrum through Fourier transform. The axial resolution was estimated to be $8.4 \mu\text{m}$ through curve fitting. The theoretical axial resolution determined by coherence gating was estimated to be $5.9 \mu\text{m}$ ($\delta z = 0.44 \lambda_0^2 / \delta \lambda$). We evaluated the effectiveness of Gaussian fitting of the PSF using the R^2 statistics and the result was 0.97, suggesting a Gaussian model provided a satisfactory fitting. Several factors may contribute to the difference between theoretical and experimental axial resolution. First, the effective bandwidth used for interferometric imaging is smaller because of spectral dependent light attenuation by various optical components. Second, the SLM generates a discrete sinusoidal pattern to represent Eq. (2), assuming the wavenumber interval (δk) covered by each SLM pixel is a constant across all the pixels of the SLM. However, the nonlinear sampling of wavenumber by the SLM may result in a compromised axial resolution in OCT imaging [21,27]. To demonstrate OCPM's capability in measuring nanoscale optical path length variation, we imaged a resolution target (Variable Line Grating Target, Thorlabs, R1L3S6P). We obtained the phase image, converted the phase to the height ($d = \phi / (4\pi \lambda_0)$), and

show the 3D surface profile of the resolution target in Fig. 2(f). We calculated the optical path length difference between the two regions of interest (ROI1 from $x = 48 \mu\text{m}$ to $x = 55 \mu\text{m}$; ROI2 from $x = 69 \mu\text{m}$ to $x = 76 \mu\text{m}$) to estimate the thickness of the chrome layer. The result obtained is 109 nm and is consistent with the chrome thickness provided by the manufacturer (120 nm). We evaluated the transverse resolution of the OCPM system by imaging a 1951 USAF resolution target. We took OCPM measurements and obtained the amplitude image (Fig. 2(g)) and phase image. Figure 2(h) shows the 3D surface topology of the sample rendered using the phase data. The phase data in Fig. 2(h) is thresholded by the amplitude image, to suppress the large phase noise from the glass substrate where the amplitude signal is low. As indicated by the black oval in Fig. 2(g), the imaging system can resolve the 1st element of the 9th group ($\sim 0.98 \mu\text{m}$), in x and y direction, suggesting a $0.98 \mu\text{m}$ transverse resolution. To assess the sensitivity in phase measurement, we used a mirror as the sample, matched the optical path length ($z = z_{\text{SLM}}/2$), and obtained the phase image. We selected a window at the center of the field of view. The size of the window was chosen to cover a resolution cell in the transverse plane (7-by-7 window, given $0.14 \mu\text{m}$ sampling interval and $0.98 \mu\text{m}$ resolution). Within the window, we calculated σ_ϕ , the standard deviation of the extracted phase. The experimentally measured σ_ϕ was 0.048 rad, corresponding to a 2.8 nm displacement sensitivity.

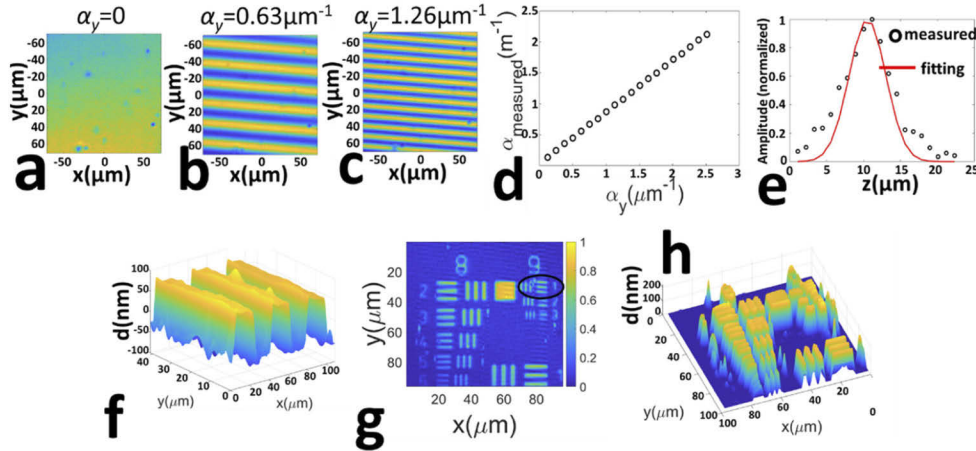


Fig. 2. (a) – (c): measurements taken by the camera when the SLM projected patterns with different α_y ; (d) α_y measured versus the value used to create SLM pattern; (e) axial PSF (circles: measurement; line: Gaussian fitting); (f) 3D surface profile of the variable light grating target; (g) amplitude image of the 1951 USAF resolution target; (h) surface profile of the resolution target rendered based on phase measurement.

After confirming the performance of OCPM on samples with well-known characteristics, we used OCPM to image live HeLa cells. Figure 3(a) – (d) show snapshot measurements taken by the camera, the amplitude image, the phase image, and the 3D surface profile of the cells. Two individual cells can be observed within the field of view. The phase image in Fig. 3(c) shows cell morphology consistent with HeLa cells observed in other quantitative phase imaging techniques [15]. Clear cell body can be observed and larger phase retardation is found at regions corresponding to the nucleus. The contrast of Fig. 3(c) is significantly higher than Fig. 3(b), because cells are highly transparent and do not alter the amplitude of incident light significantly.

We used OCPM to image the dynamics of magnetic nanoparticles attached to a live cell. We added magnetic nanoparticles to the dish where HeLa cells were cultured. We acquired 200 frames of data over a 24s time period. The imaging time was chosen such that the signal light could sufficiently saturate the sensor. To mechanically excite the nanoparticles, we translated a

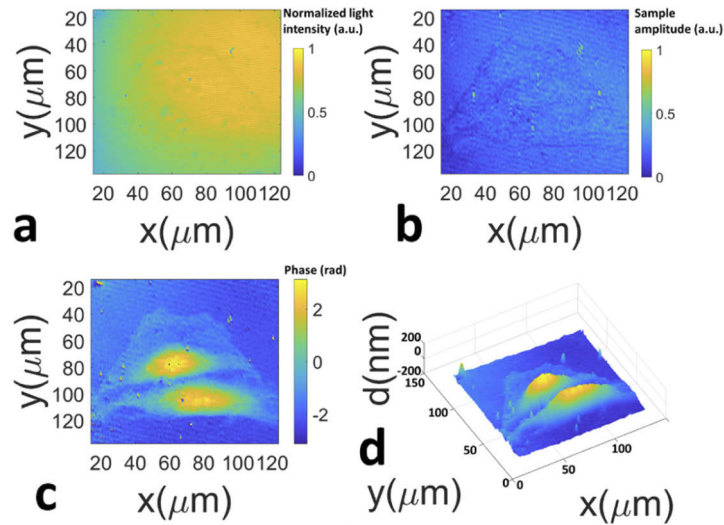


Fig. 3. (a) OCPM measurement taken from cultured HeLa cells (two cells are within the field of view); (b) amplitude image; (c) phase image; (d) 3D rendered surface profile of the cells.

permanent magnet (Neodymium Magnets) along the direction of light propagation periodically (1 Hz). Figure 4(a) and (b) show amplitude and phase images obtained from one OCPM measurement. In Fig. 4(a), regions corresponding to nanoparticle clusters (indicated by the arrows) show reduced signal magnitude, because of light attenuation induced by nanoparticles. The size of the nanoparticle cluster was in the order of $10\ \mu\text{m}$ and we did not intend to image individual nanoparticles. Figure 4(c) - (f) show the 3D surface profiles of the cell rendered using phase images. As indicated by the arrows, the surface topology changed over time due to the motion of the nanoparticles. To highlight the dynamic imaging capability of OCPM, we performed Doppler analysis on the phase images obtained. For each pixel of the phase image, we calculated the phase difference ($\delta\phi(t) = \phi(t) - \phi(t - \delta t)$) between the current frame and the previous frame. The result is similar to Doppler signal widely used to track instantaneous motion. For display, we denoted a positive phase shift using color red and a negative phase shift using color green, and overlaid the Doppler image with grayscale amplitude image (Fig. 4(g) and (h) for the 135th and 143th frame). The Doppler image for the entire measurement sequence is shown in Visualization 1. We selected two regions of interest (ROIs, 3-pixel by 3-pixel) that are indicated by the black arrow (with nanoparticles) and the asterisk (nanoparticles) in Fig. 4(b). We converted phase shift within the ROIs to instantaneous velocity along the axial direction ($v(t) = \delta\phi(t)\lambda_0 / (4\pi\delta t)$). We show the velocity estimation within both ROIs in Fig. 4(i) (black curve: ROI with nanoparticles; blue curve: ROI without nanoparticles). Figure 4(i) shows a larger magnitude of axial motion for the region covered by nanoparticle clusters. We performed Fourier analysis on the traces of motion and show the results in Fig. 4(j). The result obtained from the region with nanoparticles (black curve) shows a peak at 1 Hz that was the frequency of external magnetic excitation, while the result obtained from the other region (blue curve) does not show such a peak.

We also used OCPM to image the dynamics of cells driven by magnetic nanoparticles. We added Trypsin, a serine protease that breaks down the proteins which enable cell adhesion, to the cell culturing medium to introduce cell detachment and waited until the cells fully detached from the substrate of the culture dish to take a spherical geometry [28]. We show the amplitude and phase images of the sample in Fig. 5(a) and (b). In Fig. 5(a), a fully detached cell has a circular

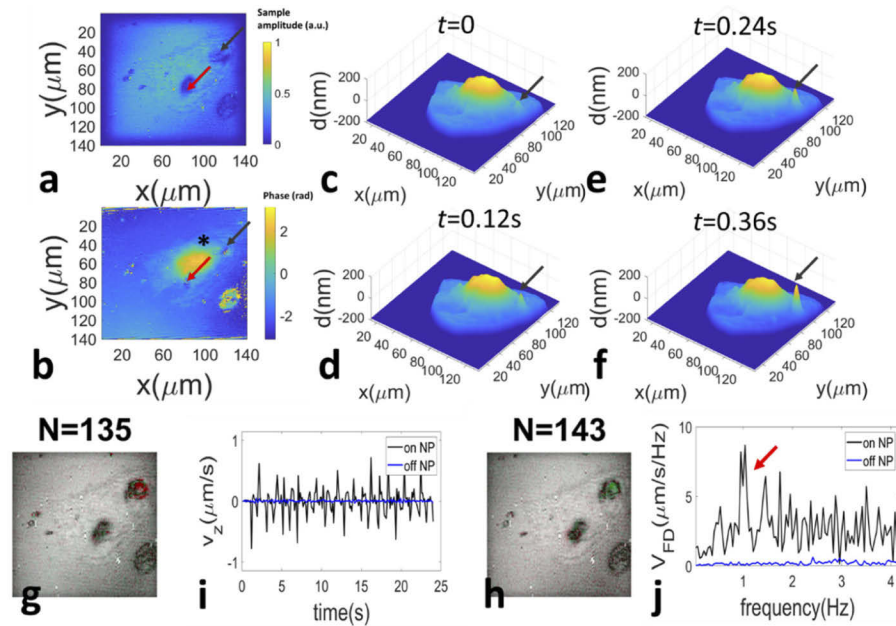


Fig. 4. (a) amplitude image of a HeLa cell and clusters of nanoparticles (arrows) sedimented to the surface of the cell; (b) phase image; (c) - (f) 3D surface profiles show the motion of nanoparticles (arrows); (g) - (h) overlaid amplitude image and Doppler image that show the motion of the nanoparticles; (i) axial velocity assessed for regions with (black) and without (blue) nanoparticles; (j) Fourier analysis of axial velocity shown in Fig. 4(g).

shape (red arrows). The cluster of nanoparticles corresponds to a region with lower amplitude (black arrow), similar to results shown in Fig. 4(a). In the phase image (Fig. 5(b)), the detached cells (red arrows) show alternating colors (yellow to blue and blue to yellow) along the direction of the phase gradient. This is the phase wrapping artifact that arises due to a phase variation beyond the range of $[-\pi, \pi]$. To excite motion, we used an external magnetic field to drive the nanoparticles, with the same approach utilized to obtain Fig. 4. We took OCPM measurements (200 frames), reconstructed the phase images, and calculated the phase shift to obtain the Doppler images that quantify instantaneous motion velocity (z direction). We overlaid the amplitude image and Doppler image in Fig. 5(c) (the 53rd frame). As shown in Fig. 5(c), the detached cell in proximity to the nanoparticle cluster had a large magnitude of motion, while other cells did not move significantly. The Doppler analysis results for the entire measurement sequence are shown in Visualization 2. Notably, the Doppler phase shift is positive (red) in half of the cell and negative (green) in the other half. This implies the cell did translate linearly. Instead, when the cell is mechanically disturbed, it rolls on the surface, resulting in positive axial velocity at one half of the sphere and negative velocity at the other half of the sphere as indicated in Fig. 5(d). To further illustrate this, we selected two pairs of frames from the sequence of Doppler images (without amplitude overlay). We show the region corresponding to the same moving HeLa cell in Fig. 5(e) and (f). In the 16th and 52nd Doppler images, we show the location the cell before and after displacement (dashed circle and solid circle), and the motion in the transverse plane (white arrow). Results in Fig. 5 suggest that OCPM can be used to quantitatively study the complicated motion of freely moving cells.

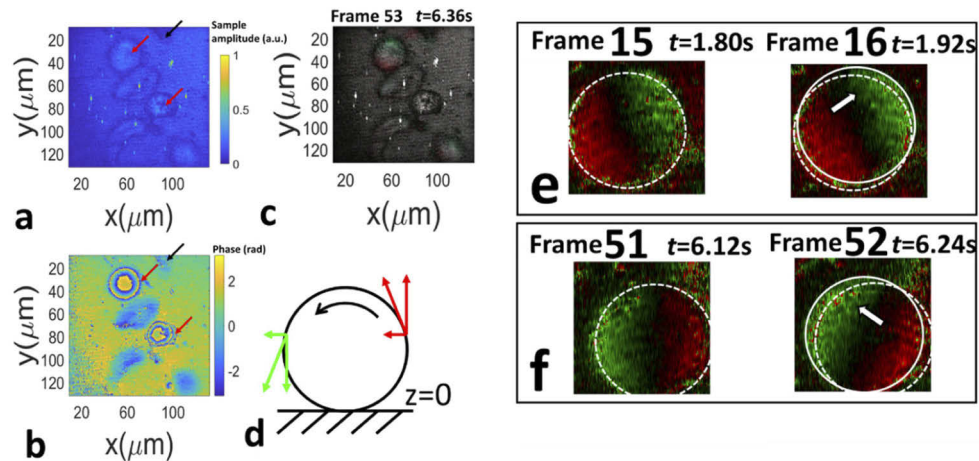


Fig. 5. (a) amplitude image and (b) phase image obtained from a culture dish with detached HeLa cells and magnetic nanoparticles; (c) a frame of Doppler image that quantifies the instantaneous motion; (d) the motion of the detached cell is similar to a ball on a rigid surface; (e) – (g) adjacent frames of Doppler image. The red arrows indicate a detached HeLa cells; the black arrow indicates a nanoparticle cluster that was driven mechanically with external magnetic field; the white arrows indicate the transverse displacement taken by the cell between frames displaced.

5. Conclusion and discussion

In summary, we built and validated the OCPM system that uses optical computation to process 3D spatial-spectral data before 2D detection. We demonstrated OCPM's capability in quantitative phase imaging of cells interacting with non-transparent magnetic nanoparticles. The cell morphology measurement (Fig. 3) was correlated with published results. Results in Fig. 4 and (5) are unique. We demonstrated phase resolved imaging to track the motion of magnetic nanoparticles under external magnetic field excitation for the first time to our best knowledge. There is also no previous study on Doppler tracking of cellular motion under mechanical excitation.

We chose to demonstrate the dynamic imaging capability of OCPM using magnetic nanoparticles, because these nanoparticles move under external magnetic excitation and can be unambiguously identified. For the nanoparticle clusters, the motion (Fig. 4) depended on their magnetic properties, the external magnetic field, and the mechanical properties of the environment (cell and cell culturing medium). We did not intend to perform theoretical calculation of the motion which is extremely challenging. Instead, we compared regions with and without nanoparticles (Fig. 4(i) and (j)), and correlated the frequency characteristics of the velocity with the alternating frequency of magnet field (Fig. 4(j)), to validate the motion was indeed excited by the magnetic field. One unique feature of OCPM is its depth resolution. With depth resolution, OCPM has the capability to resolve a thin layer from a bulk object, and is translatable to *in vivo* applications on animals or humans. The depth resolution in OCPM also implies a higher sensitivity to local motion. Conventional phase imaging techniques operate in a transmission mode and measure the phase delay along the entire trajectory of light propagation. In OCPM, the signal comes from a specific resolution cell and the phase quantifies location of scattering center for the particular resolution cell. When the sample has a subtle motion, the scattering center displaces and results in a measurable phase shift.

We anticipate OCPM to become a powerful instrument that enables scientific discoveries. One of the most significant advantages of OCPM is its label free imaging capability. At the same time,

the fast recording of OCPM also permits the monitoring of fast dynamics, including cell migration and cell proliferation. As a proof-of-concept, we showed that OCPM enables quantitative imaging of the dynamics when cells interact with nanoparticles. As shown in Fig. 4 and 5, OCPM reveals the morphology, optical properties, and motion of the microscopic objects. Particularly, our results show the size of the nanoparticle clusters and provide quantitative measure of magnetic field induced motion. Following a similar experimental approach, OCPM can be used to visualize and track varied nanoparticles and track how the cells uptake these nanoparticles over time. With an increasing number of FDA approved cases of nanoparticle drug delivery systems, we anticipate great potential of our technique in this field, as the cell-nanoparticle interactions are important factors to achieve efficiency and safe drug delivery. OCPM function can be added to a generic microscope, by adding a reference arm to create interference and inserting an optical computation module (Fig. 1(b)) between the interferometer and the camera. Hence the technology can be easily integrated with existing microscopy technologies for biomedical studies.

OCPM is different from conventional phase imaging techniques in its contrast mechanism, because it has depth resolution derived from low coherence interferometry and optical computation. According to Eq. (6), the optical computation module determines the imaging depth ($z_{SLM}/2$). OCPM operated in a reflective mode can image weakly scattering objects such as cultured cells and scattering objects such as. OCPM can also resolve a thin layer from a bulk object that is nontransparent and scatters light. Therefore, OCPM operated in a reflective mode is translatable to in vivo applications on animals or human subjects. In comparison, it is challenging to perform in vivo imaging using a phase imaging system operated a transmission mode. The depth resolution in OCPM also enables Doppler analysis, which is critical for quantitative motion tracking. In OCPM, the phase effectively quantifies the optical path length of light from the center of the scattering field within the selected resolution cell. When the sample moves, the mass within the resolution cell moves and the equivalent center of the scattering field displaces to result in a measurable phase shift. In comparison, a phase imaging system that operates in a transmission mode measures the phase delay along the entire trajectory of light propagation. In addition, OCPM is different from other phase measurement techniques based on low coherence interferometry such as phase resolved OCT, because the waveform used for phase calculation does not come from interference. Instead, the fringe used to calculate the phase is created by optical computation. When a low coherence light source is used, it is challenging to form a dense interference fringe in an extended area, while a denser fringe is needed for high resolution phase measurement. In OCPM, the “apparent fringe” is determined by SLM modulation in y dimension (Eq. (2) and Fig. 2(a) – (c)). Therefore, we were able to control the density of the fringe pattern using the parameter α_y , and achieve a high transverse resolution ($\sim 0.98 \mu\text{m}$), although a broadband source with extended emission area (LED) was used to illuminate the interferometer. Nevertheless, the approach utilized to create fringe along y dimension is different from direct amplitude modulation. As suggested by Eq. ((6)), the modulation is only applied to signal from the resolution cell located at ($z_{SLM}/2$). Experimentally, if the sample is located at a different depth, fringe along y dimension simply does not appear.

Funding. National Institute of General Medical Sciences (1 R21 GM140438-01).

Disclosures. The authors declare no conflicts of interest.

Data availability. Data underlying the results presented in this paper are not publicly available at this time but may be obtained from the authors upon reasonable request.

References

1. J. K. Patra, G. Das, L. F. Fraceto, E. V. R. Campos, M. d. P. Rodriguez-Torres, L. S. Acosta-Torres, L. A. Diaz-Torres, R. Grillo, M. K. Swamy, S. Sharma, S. Habtemariam, and H.-S. Shin, “Nano based drug delivery systems: recent developments and future prospects,” *J. Nanobiotechnol.* **16**(1), 71 (2018).
2. J. C. Kraft, J. P. Freeling, Z. Wang, and R. J. Ho, “Emerging research and clinical development trends of liposome and lipid nanoparticle drug delivery systems,” *J. Pharm. Sci.* **103**(1), 29–52 (2014).

3. X. Hou, T. Zaks, R. Langer, and Y. Dong, "Lipid nanoparticles for mRNA delivery," *Nat. Rev. Mater.* **6**(12), 1078–1094 (2021).
4. S. Ashraf, A. Hassan Said, R. Hartmann, M.-A. Assmann, N. Feliu, P. Lenz, and W. J. Parak, "Quantitative Particle Uptake by Cells as Analyzed by Different Methods," *Angew. Chem. Int. Ed.* **59**(14), 5438–5453 (2020).
5. F. Zernike, "How I discovered phase contrast," *Science* **121**(3141), 345–349 (1955).
6. R. Allen and G. David, "The Zeiss-Nomarski differential interference equipment for transmitted-light microscopy," *Z. Wiss. Mikrosk.* **69**, 193–221 (1969).
7. D. Huang, E. A. Swanson, C. P. Lin, J. S. Schuman, W. G. Stinson, W. Chang, M. R. Hee, T. Flotte, K. Gregory, and C. A. Puliafito, "Optical coherence tomography," *Science* **254**(5035), 1178–1181 (1991).
8. Y. Zhao, Z. Chen, C. Saxer, S. Xiang, J. F. de Boer, and J. S. Nelson, "Phase-resolved optical coherence tomography and optical Doppler tomography for imaging blood flow in human skin with fast scanning speed and high velocity sensitivity," *Opt. Lett.* **25**(2), 114–116 (2000).
9. B. Vakoc, S.-H. Yun, J. De Boer, G. Tearney, and B. Bouma, "Phase-resolved optical frequency domain imaging," *Opt. Express* **13**(14), 5483–5493 (2005).
10. X. Liu, F. R. Zaki, H. Wu, C. Wang, and Y. Wang, "Temporally and spatially adaptive Doppler analysis for robust handheld optical coherence elastography," *Biomed. Opt. Express* **9**(7), 3335–3353 (2018).
11. A. Dubois, J. Selb, L. Vabre, and A.-C. Boccara, "Phase measurements with wide-aperture interferometers," *Appl. Opt.* **39**(14), 2326–2331 (2000).
12. A. Dubois, L. Vabre, A.-C. Boccara, and E. Beaufort, "High-resolution full-field optical coherence tomography with a Linnik microscope," *Appl. Opt.* **41**(4), 805–812 (2002).
13. G. Popescu, L. P. Deflores, J. C. Vaughan, K. Badizadegan, H. Iwai, R. R. Dasari, and M. S. Feld, "Fourier phase microscopy for investigation of biological structures and dynamics," *Opt. Lett.* **29**(21), 2503–2505 (2004).
14. T. Ikeda, G. Popescu, R. R. Dasari, and M. S. Feld, "Hilbert phase microscopy for investigating fast dynamics in transparent systems," *Opt. Lett.* **30**(10), 1165–1167 (2005).
15. N. Lue, W. Choi, G. Popescu, T. Ikeda, R. R. Dasari, K. Badizadegan, and M. S. Feld, "Quantitative phase imaging of live cells using fast Fourier phase microscopy," *Appl. Opt.* **46**(10), 1836–1842 (2007).
16. T. H. Nguyen, C. Edwards, L. L. Goddard, and G. Popescu, "Quantitative phase imaging with partially coherent illumination," *Opt. Lett.* **39**(19), 5511–5514 (2014).
17. Y. Park, C. Depeursinge, and G. Popescu, "Quantitative phase imaging in biomedicine," *Nat. Photonics* **12**(10), 578–589 (2018).
18. Y. Cotte, F. Toy, P. Jourdain, N. Pavillon, D. Boss, P. Magistretti, P. Marquet, and C. Depeursinge, "Marker-free phase nanoscopy," *Nat. Photonics* **7**(2), 113–117 (2013).
19. J. M. Soto, A. Mas, J. A. Rodrigo, T. Alieva, and G. Domínguez-Bernal, "Label-free bioanalysis of *Leishmania infantum* using refractive index tomography with partially coherent illumination," *J. Biophotonics* **12**(9), e201900030 (2019).
20. J. M. Soto, J. A. Rodrigo, and T. Alieva, "Partially coherent optical diffraction tomography toward practical cell study," *Front. Phys.* **9**, 320 (2021).
21. Y. Wang, Q. Kang, Y. Zhang, and X. Liu, "Optically computed optical coherence tomography for volumetric imaging," *Opt. Lett.* **45**(7), 1675–1678 (2020).
22. D. R. Solli and B. Jalali, "Analog optical computing," *Nat. Photonics* **9**(11), 704–706 (2015).
23. W. Zhang, X. Zhang, C. Wang, W. Liao, S. Ai, J. Hsieh, N. Zhang, and P. Xue, "Optical computing optical coherence tomography with conjugate suppression by dispersion," *Opt. Lett.* **44**(8), 2077–2080 (2019).
24. Z. Zhang, X. Ma, and J. Zhong, "Single-pixel imaging by means of Fourier spectrum acquisition," *Nat. Commun.* **6**(1), 6225 (2015).
25. C. Maurer, A. Jesacher, S. Bernet, and M. Ritsch-Marte, "What spatial light modulators can do for optical microscopy," *Laser Photonics Rev.* **5**(1), 81–101 (2011).
26. H. Iida, K. Takayanagi, T. Nakanishi, and T. Osaka, "Synthesis of Fe₃O₄ nanoparticles with various sizes and magnetic properties by controlled hydrolysis," *J. Colloid Interface Sci.* **314**(1), 274–280 (2007).
27. X. Liu, M. Balicki, R. H. Taylor, and J. U. Kang, "Towards automatic calibration of Fourier-domain OCT for robot-assisted vitreoretinal surgery," *Opt. Express* **18**(23), 24331–24343 (2010).
28. S. J. Weiner, G. L. Seibel, and P. A. Kollman, "The nature of enzyme catalysis in trypsin," *Proc. Natl. Acad. Sci. U. S. A.* **83**(3), 649–653 (1986).